KeA1

CHINESE ROOTS
GLOBAL IMPACT

Contents lists available at ScienceDirect

Petroleum Science

journal homepage: www.keaipublishing.com/en/journals/petroleum-science



Original Paper

Pore network modeling of gas—water two-phase flow in deformed multi-scale fracture-porous media



Dai-Gang Wang ^{a, b, *}, Yu-Shan Ma ^a, Zhe Hu ^a, Tong Wu ^c, Ji-Rui Hou ^a, Zhen-Chang Jiang ^d, Xin-Xuan Qi ^a, Kao-Ping Song ^a, Fang-Zhou Liu ^{a, **}

- ^a State Key Laboratory of Petroleum Resources and Engineering, China University of Petroleum, Beijing, 102249, China
- ^b State Key Laboratory of Deep Oil and Gas, China University of Petroleum (East China), Qingdao, 266580, Shandong, China
- ^c Research Institute of Petroleum Exploration and Development, PetroChina, Beijing, 100083, China
- d Research Institute of Exploration and Development, Jilin Oilfield Company of PetroChina, Songyuan, 138000, Jilin, China

ARTICLE INFO

Article history: Received 4 August 2024 Received in revised form 21 March 2025 Accepted 22 March 2025 Available online 24 March 2025

Edited by Yan-Hua Sun

Keywords:
Ultra-deep reservoir
In-situ stress loading
U-Net fully convolutional neural network
CT scanning
Microstructure deformation
Pore-scale fluid flow

ABSTRACT

Two actual rocks drilled from a typical ultra-deep hydrocarbon reservoir in the Tarim Basin are selected to conduct in-situ stress-loading micro-focus CT scanning experiments. The gray images of rock microstructure at different stress loading stages are obtained. The U-Net fully convolutional neural network is utilized to achieve fine semantic segmentation of rock skeleton, pore space, and microfractures based on CT slice images of deep rocks. The three-dimensional digital rock models of deformed multiscale fractured-porous media at different stress loading stages are thereafter reconstructed, and the equivalent fracture-pore network models are finally extracted to explore the underlying mechanisms of gas-water two-phase flow at the pore-scale. Results indicate that, in the process of insitu stress loading, both the deep rocks have experienced three stages; linear elastic deformation, nonlinear plastic deformation, and shear failure. The micro-mechanical behavior greatly affects the dynamic deformation of rock microstructure and gas-water two-phase flow. In the linear elastic deformation stage, with the increase in in-situ stress, both the deep rocks are gradually compacted, leading to decreases in average pore radius, pore throat ratio, tortuosity, and water-phase relative permeability, while the coordination number nearly remains unchanged. In the plastic deformation stage, the synergistic influence of rock compaction and existence of micro-fractures typically exert a great effect on pore-throat topological properties and gas-water relative permeability. In the shear failure stage, due to the generation and propagation of micro-fractures inside the deep rock, the topological connectivity becomes better, fluid flow paths increase, and flow conductivity is promoted, thus leading to sharp increases in average pore radius and coordination number, rapid decreases in pore throat ratio and tortuosity, as well as remarkable improvement in relative permeability of gas phase and

© 2025 The Authors. Publishing services by Elsevier B.V. on behalf of KeAi Communications Co. Ltd. This is an open access article under the CC BY-NC-ND license (http://creativecommons.org/licenses/by-nc-nd/4.0/).

1. Introduction

In last decades, the China's demand for hydrocarbon has continued to grow with external dependency on crude oil and natural gas reaching 71.2% and 40.2% in 2022, respectively. The development of shallow and medium-depth hydrocarbon

E-mail addresses: dgwang@cup.edu.cn (D.-G. Wang), lfzhouu@163.com (E-Z. Liu).

resources can no longer meet China's serious energy demand. The field of hydrocarbon exploration and development has rapidly extended to the deep and ultra-deep oil and gas reservoirs of a depth of more than 4500 m, and great breakthroughs have been made in the Tarim Basin, Junggar Basin, and Sichuan Basin of China (Ma et al., 2024). Deep and ultra-deep oil and gas reservoirs have become important replacement fields for onshore hydrocarbon exploitation due to their abundant reserves, respectively 26.6 billion tons of oil and 50 trillion cubic meters of natural gas, accounting for 21% and 55% of the total hydrocarbon resources in China. However, the degrees of oil and gas exploration are relatively

^{*} Corresponding author.

^{**} Corresponding author.

low, only 13% for oil and 10% for natural gas. Especially, there are more than 10 billion tons of deep and ultra-deep hydrocarbon resources distributed in the Tarim Basin and Junggar Basin while only 1.66 billion tons of reserves is proven, providing a strong energy guarantee to stabilize China's oil and gas strategy (Hao, 2022).

The deep and ultra-deep hydrocarbon reservoirs are typically characterized by high temperature and high pressure, strong geostress, and severe heterogeneity. Compared to the shallow and medium-depth hydrocarbon reservoirs, the temperature of deep and ultra-deep hydrocarbon reservoirs is generally above 150 °C. The reservoir matrix is ultra-low permeability or tight, and various high-angle fractures are widely distributed. It is because of the severe advance of active formation water along fractures that results in the average recovery factor usually less than 15%. Due to the influence of strong geo-stress, the flow—solid coupling effect is also significant (Sun et al., 2013; Yao et al., 2018). With continuous exploitation of oil and gas in this type of reservoirs, formation pressure gradually decreases and effective stress increases, typically leading to dynamic deformation of rock microstructure and fracture morphology (Sun et al., 2020; Wang et al., 2024; Yao et al., 2023). This phenomenon can greatly affect the fluid flow in porous media (Galkin et al., 2022; Martyushev et al., 2023). It is of great significance to study the fluid flow in in deformed multi-scale fracture-pore media so as to understand the non-uniform water invasion in fractures and provide insights to the efficient development of this type of reservoirs.

In order to visually study the effect of effective stress, flow, and chemistry on rock structure, different types of stress-loading CT scanning devices are developed, such as uniaxial loading and triaxial loading (Rassouli and Lisabeth, 2021; Van Stappen et al., 2018). Among them, the triaxial stress loading CT is often used to simulate ultra-high-pressure conditions for real-time monitoring of rock microstructure deformation and fracture propagation caused by in-situ stress loading. Ju et al. (2018) and Mao et al. (2023) have conducted extensive works on the deformation of rock microstructure. They combined an in-situ triaxial stress-loading device with efficient digital volume correlation (DVC) methods to characterize the fracture morphology and rock microstructure deformation of coal, concrete, and other specimens under dynamic stress-strain loading. Lenoir et al. (2007) utilized in-situ stressloading micro-focus CT with DVC method to observe the stress changes inside mudstone and analyze the characteristics of shear strain generation and evolution. Great efforts have been made by Huang et al. (2019), Renard et al. (2019), and McBeck et al. (2022) to reveal the stress changes within sandstone and limestone using insitu triaxial loading CT, and analyze the generation, evolution, and interaction of localized regions under expansion, compression, and shear strain. In addition, Rassouli and Lisabeth (2021) and Shi et al. (2021) also conducted in-situ scanning of shale and hard clay rocks under uniaxial compression to observe the evolution of localized strain regions with load and creep time, as well as the influence of rock microstructure on their growth. It can be concluded that, using an in-situ stress-loading micro-focus CT, the gray images of microfractures and pore structure inside rocks under different dynamic loading stages can be obtained to characterize the deformation of fracture morphology and rock microstructure. The reconstructed three-dimensional digital rock models of deformed porous media will also provide an efficient basis for studying multi-phase fluid flow at the pore scale under different stress loading stages.

The pore-scale simulation methods widely used for fluid flow include pore network simulation, lattice Boltzmann method (LBM), volume of fluid (VOF) method, level set, and phase field, etc. (Zhao et al., 2019). Except for pore network simulation, the other methods are classified as "direct numerical simulation (DNS)". The pore network model has the advantages of being repeatable and

quantifiable (Guo et al., 2024; Liu et al., 2024). By performing geometric topological equivalent of the real pore structure of rocks and using the intrusion percolation theory, the semi-analytical solutions to complex physical and chemical processes are involved in micro/nano-scale fluid flow with high computational efficiency. LBM is a mesoscopic method that directly starts from a discrete model and constructs a bridge between macro and micro. continuous and discrete based on the molecular kinetics and statistical mechanics (Su et al., 2022; Wang et al., 2018). The superior advantages of LBM include simple description of fluid interaction, easy boundary definition, and straightforward programming. The other DNS methods are based on the discrete scheme of Navier-Stokes equations for multiphase flow. The more fluid components, the more complex the calculation. As the simulation domain become larger, it is more difficult to track fluid interface when using the DNS methods described above (Wang et al., 2023).

The above analysis indicates that challenges remain in accurately simulating gas—water two-phase flow in cores under varying stress conditions. These limitations hinder a complete understanding of gas-water two-phase flow behavior in ultra-deep reservoirs. To address these challenges, this study takes two actual rocks drilled from a typical ultra-deep hydrocarbon reservoir in the Tarim Basin as examples. In-situ stress-loading micro-focus CT scanning experiments are conducted to obtain CT gray images of rock microstructure under different dynamic loading stages. The U-Net fully convolutional neural network is utilized to achieve accurate semantic segmentation of rock skeleton, pore space, and fractures with the in-situ stress loading. The 3-D digital rock models of deformable multi-scale fracture-porous media are thereafter reconstructed to analyze the deformation of deep rock microstructure during in-situ stress loading. Based on the deformed multi-scale fracture-pore network models, underlying mechanisms of gas-water two-phase flow under different stress stages are investigated.

2. In-situ stress-loading micro-focus CT scanning experiment

2.1. Experimental apparatus

The in-situ stress loading CT scanning experiment is conducted using an Xradia 520 Versa 3D X-ray micro-focus CT system, as shown in Fig. 1. This equipment has superior flexibility and can achieve 3-D non-destructive X-ray imaging with a micron resolution. The X-ray micro-focus CT utilizes a two-stage magnification in the process of experiment: the first stage is geometric magnification (similar to the traditional CT), and the second stage is optical

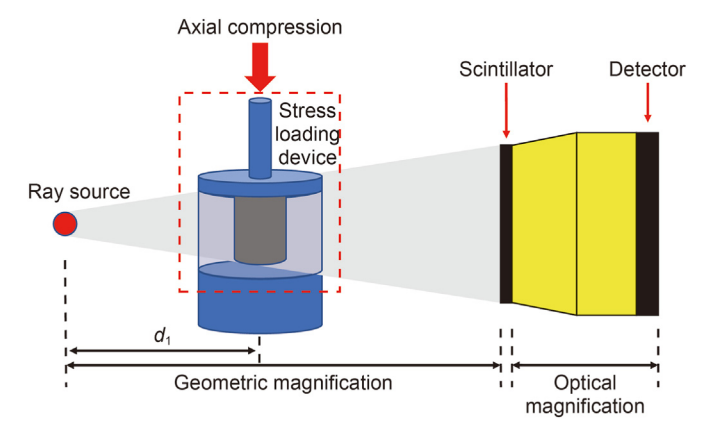


Fig. 1. Schematic of the in-situ stress-loading micro-focus CT scanning system.

magnification (similar to the synchrotron radiation CT). The two-stage magnification significantly reduces the dependence on geometric position. High-resolution CT images can be obtained even if the rock is away from the light source. The maximum allowable pressure of this device is 5000 N, which corresponds to a maximum stress of 398 MPa for cylindrical specimens with a diameter of 4 mm. The loading mode can be controlled by a constant displacement rate ranging from 0.03 to 3.0 mm/min. The compression distance varies from 15 to 5 mm between the top and bottom plate, and the test temperature range is -20 to $160\,^{\circ}\text{C}$.

In this study, the experimental rocks are drilled from a typical ultra-deep hydrocarbon reservoir in the Tarim Basin of China. Two deep rocks with different physical properties are selected for in-situ stress-loading micro-focus CT scanning to analyze the deformation of rock microstructure under different dynamic stress loading stages. The tested rock porosity is 16.1% and 16.8%, and the permeability is 10.07×10^{-3} and 57.75×10^{-3} μm^2 , respectively. Two experimental samples with a diameter of 4 mm and a length of 8 mm are further prepared from each rock. One is used for preexperiment to determine mechanical behavior and reasonable CT scanning stages, which facilitates a systematic observation of rock microstructure and fracture morphology during in-situ stress loading. The other rock sample is used for in-situ stress-loading micro-focus CT scanning with a resolution of 5.0 μm .

2.2. Experimental procedure

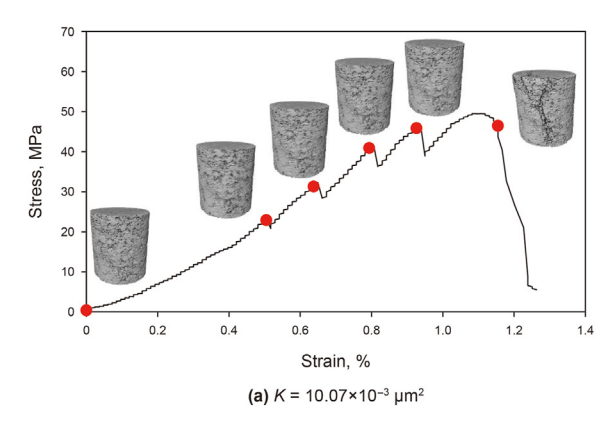
In this experiment, the stress loading device is used in conjunction with X-ray CT scanning equipment to achieve dynamic observation of deformation of rock microstructure and fracture morphology under different dynamic loading stages. The specific procedures for in-situ stress loading micro-focus CT scanning are described as follows:

- (1) Wrap the experimental rock sample to prevent it from scattering during in-situ stress loading, ensuring the acquisition of CT gray images even it is fractured.
- (2) Place the wrapped rock sample in the holder, seal it strictly, select nano-focus X-ray source, open the data acquisition software, and adjust scanning parameters such as voltage, current, and exposure time. The image resolution for this study is 5.0 μm.
- (3) Start the stress loading device, load in-situ stress at a constant displacement rate of 0.03 mm/min, observe the stress—strain change, and pause the loading when a certain stress condition is achieved, and conduct micro-focus CT scan.

- (4) Perform micro-focus CT scanning using a cone beam X-ray source with a cone angle of 5.11°. In each scanning step, a vertical projection is recorded after the X-ray passes through the deep rock sample, and a 360° rotation at the same interval angle of 0.2° is conducted to obtain 1800 projections of the rock sample, indicating a completion of CT scan at this stress loading stage.
- (5) Continue the stress loading process at the same displacement rate and repeat steps (3) and (4) until the rock sample breaks. The Volume Graphics (VG) Studio MAX software is used to denoise and perform 3-D visualization of the CT gray image data obtained at different stress loading stages.
- (6) Record the change of stress and axial displacement of rock sample during the in-situ stress loading experiment, plot the stress—strain relationship curve, and analyze the underlying mechanical effect on the deformation of rock microstructure.

2.3. Experimental results

The stress—strain relationship curves from in-situ stress loading CT scanning experiments of two deep rocks are shown in Fig. 2, where the red dots represent the CT scanning time. Both deep rock samples experienced six stress loading stages, including four stages before the rock broke, one stage at peak stress, and one stage after the rock broke. In the initial state, there are a few large pores and micro-fractures in the upper part of the low-permeability core. Stress loading causes the core to rupture, ultimately forming a complex fracture network. In the initial state, the highpermeability core contains uniformly distributed small pores with good connectivity between pores and fractures. During the stress loading process, both fractures develop and pore structures deform in a wide range. CT images reveal that deep rock samples primarily consist of uniformly distributed small pores and micro-pores. Under high stress, these pores undergo complete fragmentation, resulting in the formation of through-going fractures, with a more significant fractured region observed in the central part of the core. In addition, for the high-permeability core, micro-fractures are first generated in some areas during stress loading, and the microfractures continue to expand to form the main fractures. It can be observed that the rock with permeability of $10.07 \times 10^{-3} \, \mu m^2$ has a peak stress of 49.53 MPa and a peak strain of 1.11%, while the peak stress and peak strain of the rock with permeability of $57.75 \times 10^{-3} \ \mu m^2$ are 46.21 MPa and 1.37%, respectively. The stress—strain curve of deep rock is consistent with that obtained for other types of specimens, mainly consisting of the linear elastic stage, plastic deformation stage, and shear failure stage. Shortly



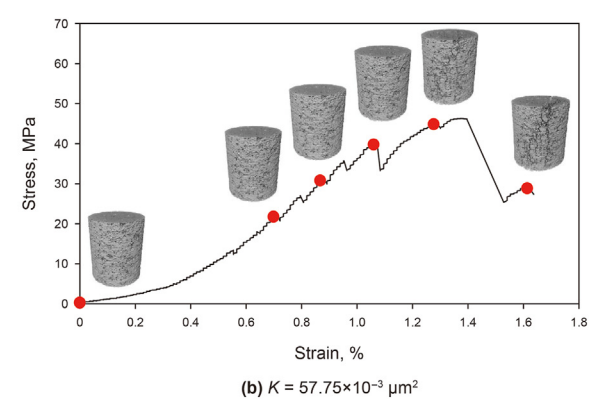


Fig. 2. The stress-strain curves of deep rocks during in-situ stress-loading micro-focus CT scanning experiments.

after one CT scan is completed, a slight drop in stress can be often monitored. This is attributed to the yield strain experienced by the rock sample under the influence of stress loading, causing the stress received by a stress sensor to be slightly lower than that before the CT scan.

3. Digital rock modeling of deformed multi-scale media

First, non-local means filtering technique (Zhang et al., 2017, 2019) is used to preprocess the CT scan slice images at different stress loading stages so as to improve the signal-to-noise ratio and clarity of the raw images. To eliminate the boundary effect as much as possible, a representative element volume (REV) with a reasonable size should be determined (Sun et al., 2019). For this study, in order to balance the accurate representation of rock microstructure and computer storage capacity, a typical cubic region of $500 \times 500 \times 900$ voxels is selected from the CT gray slice images as the REV domain, and the spatial resolution of single voxel is $5.0~\mu m$.

Image segmentation is critical for digital rock analysis, and the accuracy of image segmentation directly determines the reliability of rock microstructure description (Wang H.T. et al., 2020). The traditional image segmentation methods mainly include threshold segmentation, cluster analysis, and edge detection algorithms. Among them, the threshold segmentation algorithm has superior advantages of high operational efficiency and strong applicability (Cui et al., 2020). The principle of this method is to divide the image information into several classes based on the gray values and binarize the slice images with a gray threshold. The gray values below the threshold (a = 0) and above the threshold (a = 1)represent different classes, one of which is the valid data. The highlight areas of CT gray images represent the rock skeleton and lowlight areas indicate pore space. The effective segmentation of pore space and rock skeleton can be achieved by selecting a reasonable threshold (Chen and Xu, 2020; Saxena et al., 2017; Tan et al., 2021), as shown in Fig. 3. It can be seen that the threshold segmentation

method has a poor segmentation effect for images with similar gray values but different semantics (e.g., pore and fracture). Due to the influence of strong geo-stress, micro-pores and micro-fractures are widely distributed inside the deep rock. The gray values of these two types of reservoir space are similar, but the fluid conductivity of them differs greatly. The traditional threshold segmentation algorithm cannot effectively separate the rock skeleton, fracture, and pore space inside the deep rock at different stress-loading stages. To tackle this issue, the U-Net deep learning semantic segmentation algorithm based on a fully convolutional neural network (Dhamija et al., 2023; Du et al., 2020; Khanna et al., 2020; Zhang et al., 2023) is introduced to identify and predict the CT image data so as to accurately extract the rock skeleton, fracture, and pore information from the images during different dynamic loading stages.

In the field of image analysis, convolution is a mathematical operation. The main idea is to perform a weighted summation on local domain of input data using a convolution kernel (essentially a filter) to obtain output data. By moving this convolution kernel across the whole input data, the model can capture different semantic features within input data. The mathematical expression of convolution between function f and function g is described as:

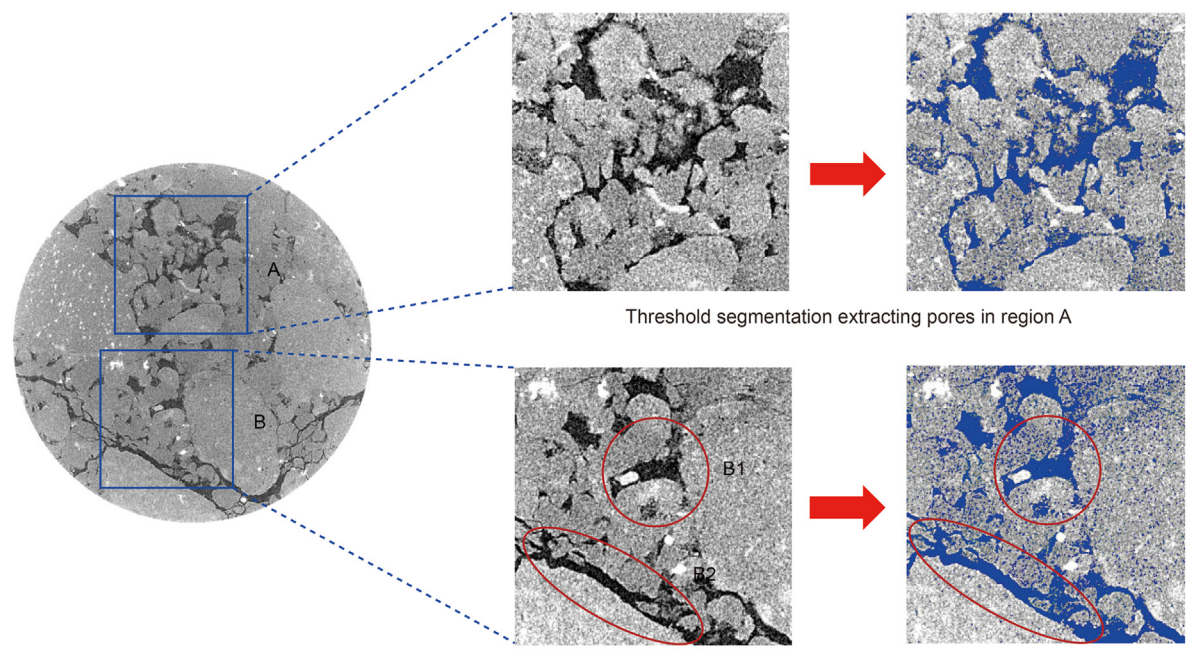
$$(f*g)(t) = \int f(\tau)g(t-\tau)d\tau \tag{1}$$

For CT scan images, each pixel is discrete, so the discrete form of convolution used in image deep learning segmentation is as follows:

$$(f*g)(t) = \sum_{a = -\infty}^{\infty} f(a)g(t - a)$$
(2)

where f is the input data which represents the pixel values in image; g is the convolution kernel which is the eigenmatrix of image.

Image deep learning semantic segmentation essentially takes the pixel values of sample images as the input function. By continuous learning and optimization, the eigenmatrix of sample



Threshold segmentation unable to extract fractures and pores with similar grayscale values

Fig. 3. Threshold segmentation of a typical CT scan slice image inside deep rock.

images is obtained, which is the convolution kernel. Through predicting input image data with the convolution kernel, the semantic segmentation of images will be achieved. A typical neural network model is composed of an input layer, hidden layers, and an output layer with each layer having specific functions. The hidden layers of a convolutional neural network primarily include the convolutional layer, pooling layer, and fully connected layer. In the convolutional layer, the convolution operation is carried out on image pixel values to obtain convolution kernel of the input image. The pooling layer is mainly used to reduce spatial resolution of the eigenmatrix, thus reducing the complexity of calculation. The fully connected layer operates on the entire eigenmatrix to map high-resolution features to output classes. Compared with traditional convolutional neural networks, the fully convolutional neural network also has a deconvolution layer, which is used to revert the low-resolution eigenmatrix to the same resolution as input image. Due to the structure of the fully convolutional neural network like the letter "U", it is also called the U-Net fully convolutional neural network. To accurately achieve multi-value segmentation of fracture, pore space and the rock skeleton, it is first necessary to use the U-Net fully convolutional neural network to learn the semantic information from CT slice images and divide the CT gray images into different classes. In order to learn the semantic information of images, it requires to establish an accurate sample space, including rock CT gray image data and the label data set. The U-Net fully convolutional neural networks mainly learn the CT gray image data and label to extract image feature information (down-sampling). Therefore, the accuracy of the sample space largely determines whether the U-Net deep learning semantic segmentation result is reliable or not. Since the information for fracture and pore structure in rock CT gray images are relatively simple, only a few CT slice images with clear fracture morphology and containing a certain number of pores are selected as the original samples. Using the Avizo digital image processing software to manually segment fracture, pore space, and rock skeleton, the sample space will be established. For this study, a typical CT slice image for deep learning and the corresponding data label are shown in Fig. 4.

An image segmentation prediction model is defined by using the deep learning TensorFlow framework, mainly including two key components: the encoder and the decoder, which are responsible for image feature extraction and segmentation (up-sampling), and a fully convolutional neural network model is ultimately established. The encoder reduces the image resolution through convolutional layer and pooling layer to capture the image feature information in the deep network while the decoder maps the low-

resolution features extracted by the encoder back to the input image. Additionally, the loss function and optimizer are two important components for constructing and training the neural network. The loss function serves as the objective function for training the neural network model. The smaller the value of the loss function, the higher the accuracy of image information. The optimizer is used to update the model parameters to gradually reduce the loss function. By training from CT slice images of the deep rock with a permeability of $10.07 \times 10^{-3} \ \mu m^2$ in the shear failure stage and the label data manually segmented, the loss function curve of the U-Net fully convolutional neural network model is shown in Fig. 5. It can be seen that during the training process, the value of the loss function value gradually decreases, and after 300 times of training, the loss function tends to be stable, indicating the end of the U-Net neural network training.

To verify the accuracy of the U-Net deep learning semantic segmentation, we compared the measured and predicted porosity of two experimental deep rocks before in-situ stress loading, as listed in Table 1. Both the relative errors of two deep rocks are below 1%, verifying the reliability of the U-Net deep learning segmentation algorithm introduced in this study. Using the marching cube method (Verri et al., 2017), the three-dimensional digital rock models of deformed multi-scale fracture-porous media under different dynamic loading stages can be constructed, which are shown in Fig. 6.

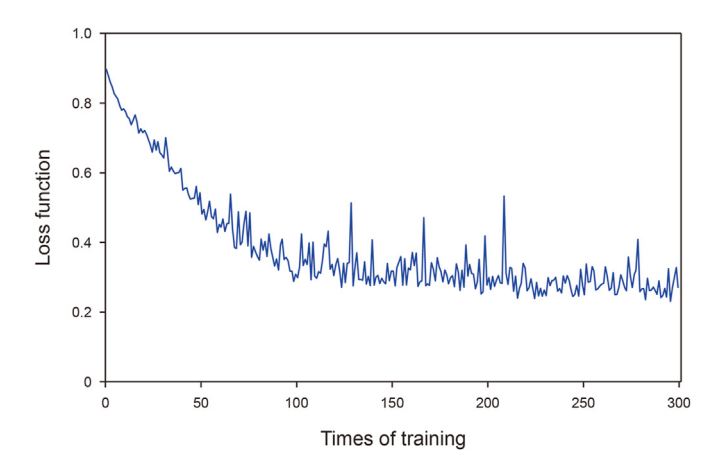


Fig. 5. Loss function curve of the U-Net neural network training.

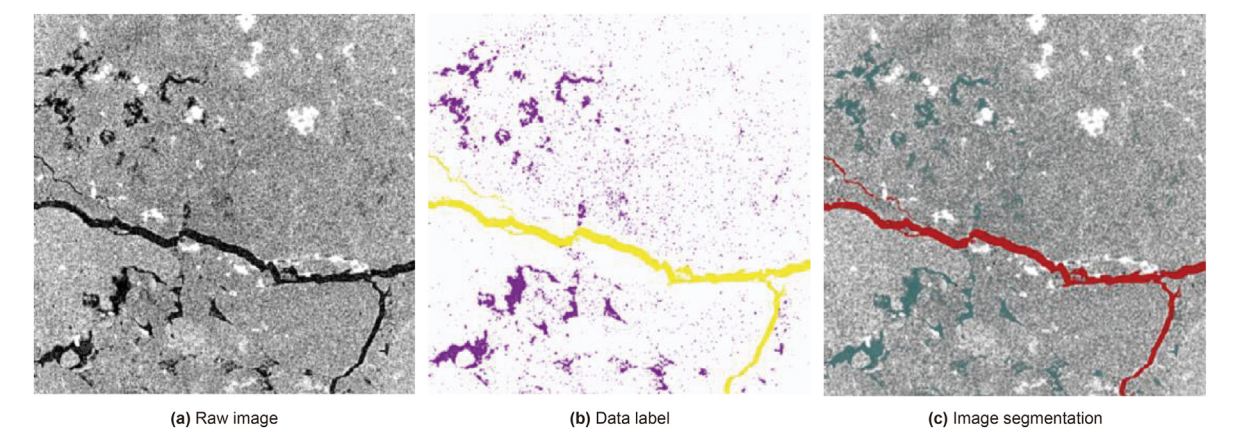


Fig. 4. Data label of a typical CT slice image by deep learning.

Table 1Validation of U-Net deep learning semantic segmentation.

Rock permeability K , $10^{-3} \mu m^2$	Rock porosity before stress loading, %		Relative error, %
	Measured value	U-Net predicted value	
10.07	0.161	0.162	0.73
57.75	0.168	0.169	0.84

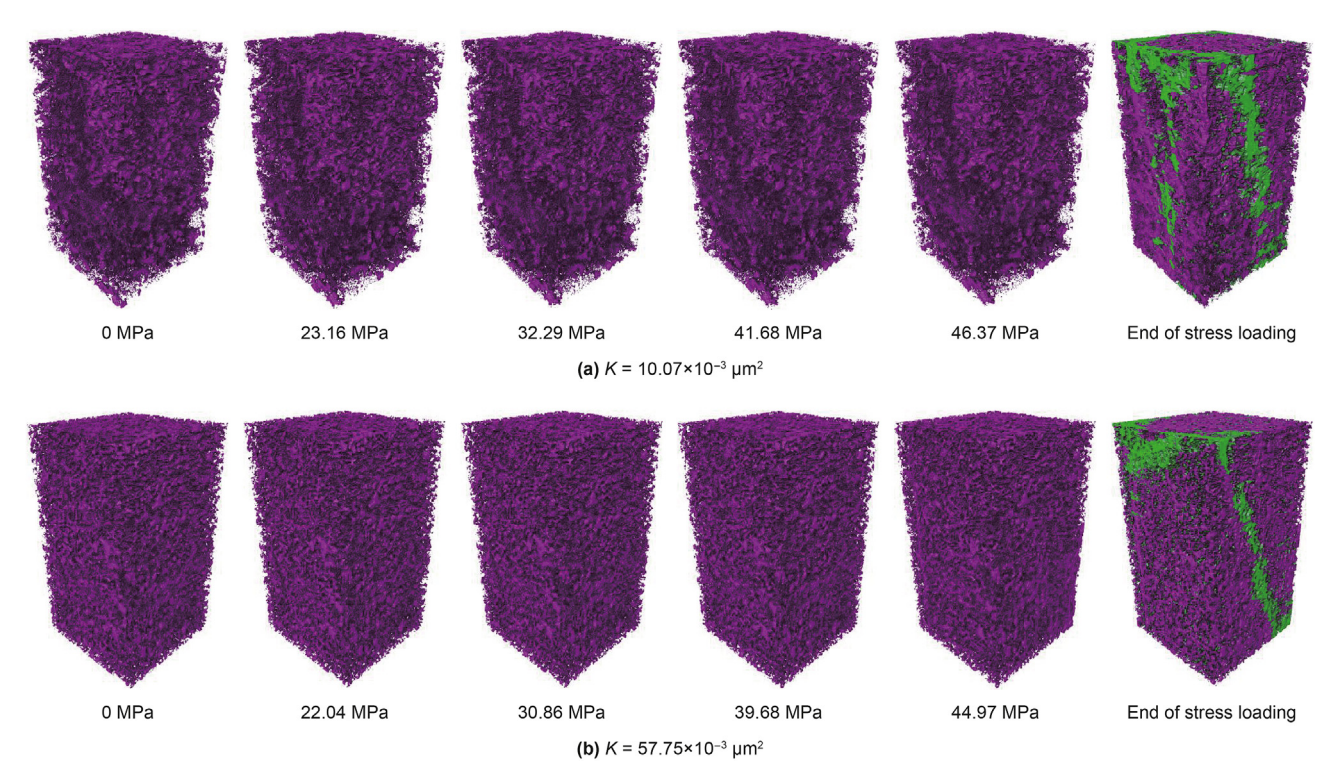


Fig. 6. 3D digital rock models of deformable multi-scale media (red: pore; green: fracture).

4. Deformation of rock microstructure induced by stress loading

In order to quantitatively evaluate the deformation evolution of deep rocks' microstructure induced by in-situ stress loading, it is necessary to determine the pore geometric properties, fracture morphology, and pore-fracture topological connectivity based on the extracted topologically equivalent 3D fracture-pore network models of the deformed multi-scale media at different dynamic loading stages. For this study, the open-source program PoreSpy is firstly used to label geometric structures of the deformed multiscale digital rocks obtained by the in-situ stress loading CT scanning experiments. The watershed algorithm (Kornilov and Safonov, 2018) is then applied to extract the topological network models of rock matrix. For the labeled micro-fractures, the central surfaces of the fractures are determined using the central axis method and the equivalent radius theory, then converting them into a virtual central axis map to extract the corresponding fracture topological networks. By satisfying the geometric properties and pore-throat connectivity, the fracture topological network is embedded into the matrix topological network under a certain stress loading stage, resulting in a hybrid 3D topological network model of the deformed multi-scale fracture-pore media, as shown in Fig. 7. The topological properties such as pore-throat ratio, coordination number and tortuosity are statistically analyzed to explore the dynamic deformation of deep rock microstructure caused by in-situ stress

loading.

Fig. 8 reflects the dynamic change in slice porosity of deep rocks during the in-situ stress-loading micro-focus CT scanning experiments. It can be observed that in the initial stage of in-situ stress loading, the slice porosity of two deep rocks decreases rapidly with the increase in in-situ stress and then gradually stabilizes at a low level until the deep rocks are fractured. This demonstrates that as the in-situ stress is loaded, the deep rocks are gradually compacted and some micro-pores are closed. The higher the in-situ stress loaded, the greater the deformation degree of deep rock microstructures. After the deep rocks are fractured in the shear failure stage, numerous micro-fractures will be generated, significantly improving the topological connectivity, thus resulting in a significant increase in the slice porosity of two deep rocks. Compared with the deep rock with a permeability of $10.07 \times 10^{-3} \, \mu \text{m}^2$, the other deep rock with a permeability of $57.75 \times 10^{-3} \, \mu m^2$ shows a larger decrease in slice porosity during the early stage of stress loading. This indicates that the better the rock properties, the more severe the deformation of rock microstructure under the same stress loading condition. When the stress exceeds 30.86 MPa, a slight increase in slice porosity can be observed, indicating the formation of a few micro-fractures inside the rock.

Fig. 9 reflects the dynamic change in pore-throat topological properties of both deep rocks under different dynamic loading stages. It indicates that the dynamic evolution of mechanical behavior of deep rock during in-situ stress loading experiments

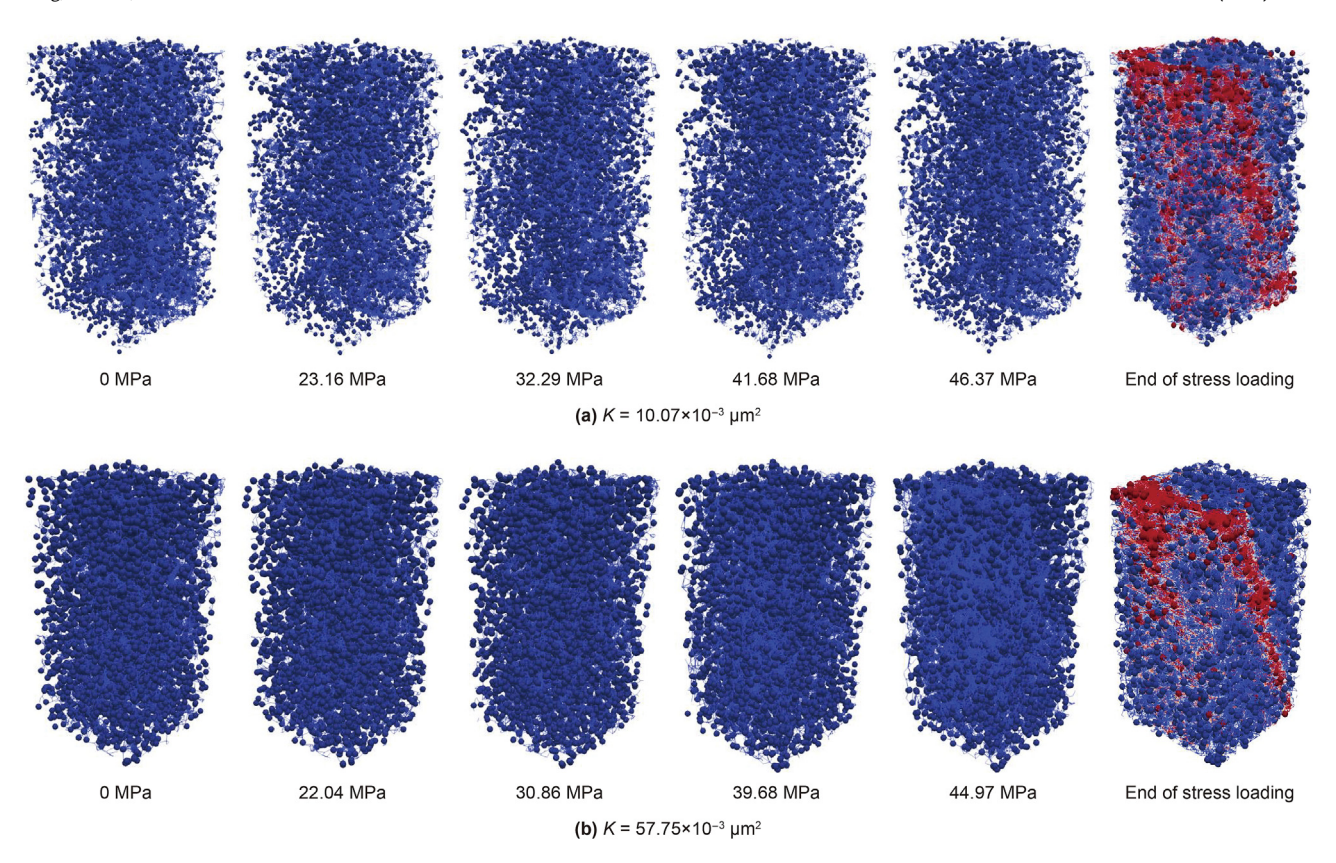


Fig. 7. Deformed multi-scale network models (blue: pore network; red: fracture network).

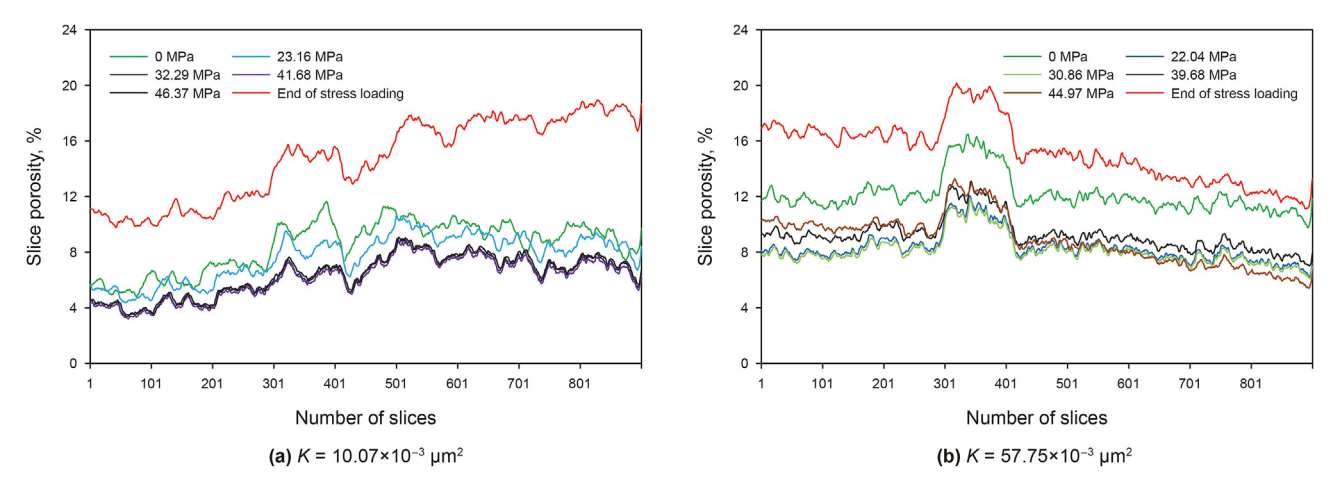


Fig. 8. Dynamic change in slice porosity of deep rocks at different stress loading stages.

significantly affects dynamic changes in the pore-throat geometric properties such as the average pore radius, pore-throat ratio, coordination number, and tortuosity. In the linear elastic deformation stage, due to rock compaction, the average pore radius, pore-throat ratio, and tortuosity of deep rocks gradually decrease, while the coordination number remains unchanged. The deep rock with a permeability of $10.07 \times 10^{-3}~\mu\text{m}^2$ experiences a relatively long linear elastic deformation stage after the initial rock compaction, and the pore-throat topological properties fluctuate slightly. The other deep rock with a permeability of $57.75 \times 10^{-3}~\mu\text{m}^2$ typically has a shorter linear elastic deformation stage and a few microfractures are generated in the plastic deformation stage, increasing the fluid flow paths inside the deep rocks. The pore-

throat ratio, coordination number, and tortuosity gradually increase with the loading of in-situ stress. After the rock is fractured, a large number of micro-fractures are generated within the deep rock, greatly improving the topological connectivity, leading to sharp increases in average pore radius and coordination number and rapid decreases in pore-throat ratio and tortuosity.

5. Microscopic gas—water flow in deformed multi-scale media

The deformable multi-scale network model can be considered as a quasi-static model (Zhang et al., 2015; Wang D.G. et al., 2020), where fluid flow is entirely dominated by capillary pressure, and

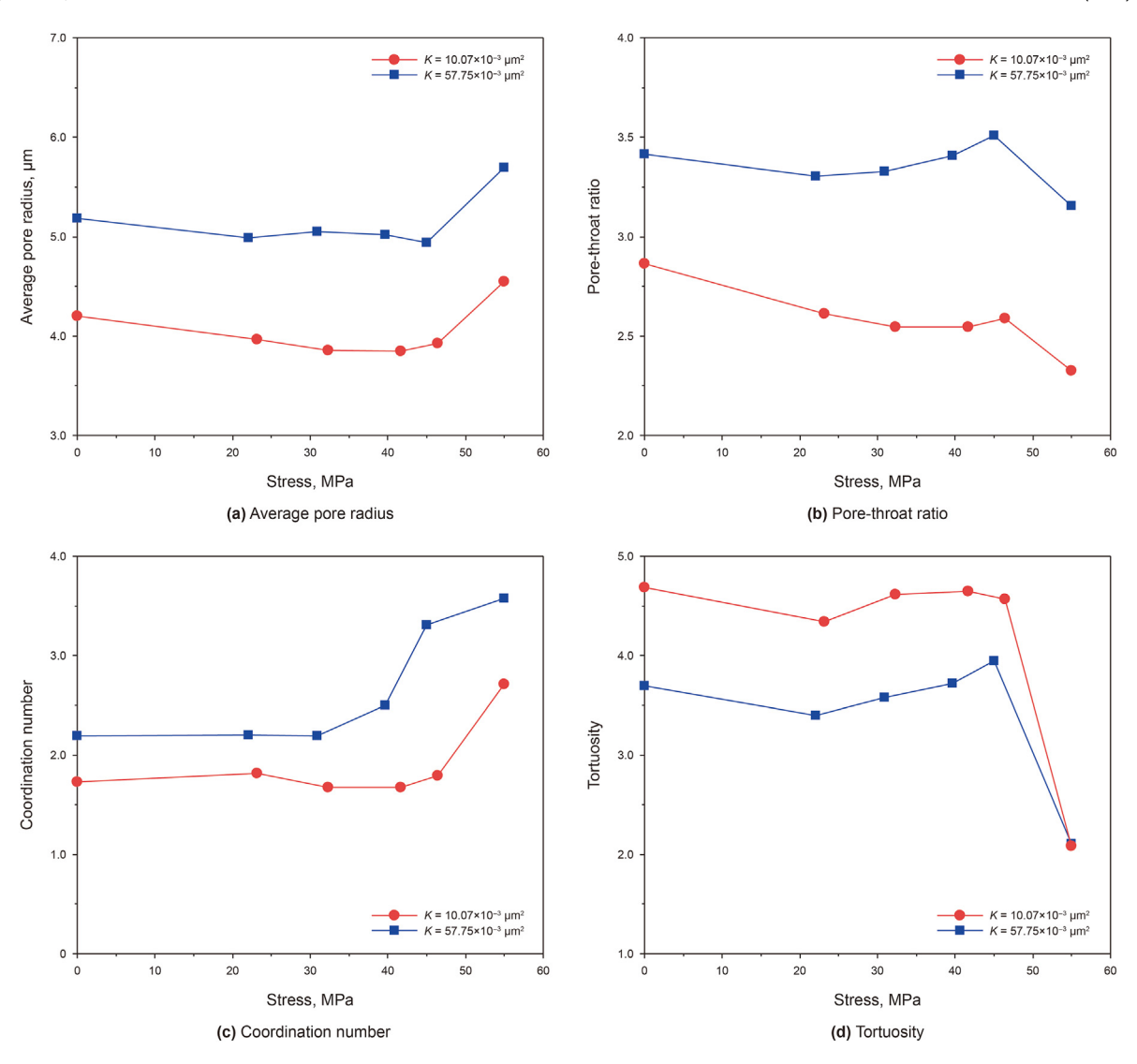


Fig. 9. Dynamic changes in pore-throat topological properties of deep rock at different stress loading stages.

the influence of viscous force on pressure drop will be ignored. Based on the extracted deformed multi-scale fracture-pore network models, the quasi-static network simulations are performed to quantify and characterize the microscopic gas—water two-phase flow in the deformed multi-scale fracture-porous media under different dynamic stress loading stages. Based on the invasion-percolation theory (Berg and Sahimi, 2023), fluid flow from one pore to another is assumed to be instantaneous, and flow within the pore-throats is typically neglected. The model is initially saturated with one fluid, and a driving pressure (P_1-P_0) is imposed. The fluid flow rate is measured to calculate absolute permeability using the Darcy equation, which is expressed as follows:

$$K = \frac{\mu QL}{A(P_1 - P_0)} \tag{3}$$

where K is the absolute permeability, μ m²; μ is the fluid viscosity, mPa·s; Q is the volumetric flow rate of the network model fully saturated with fluid phase i under a driving pressure difference (P_1-P_0) , cm³/s; A is the cross-sectional area in the direction of flow, cm².

For any pore in the deformed multi-scale network model, the

law of mass conservation must be satisfied, which implies that the volumetric flow rate that flows into the pore from the inlet throat should equal the volumetric flow rate flowing out from the outlet throat. The expression is

$$\sum_{i=1}^{z_i} q_{ij} = 0 (4)$$

$$q_{ij} = \frac{g_{ij}}{L_{ij}} \left(P_i - P_j \right) \tag{5}$$

where z_i is the coordination number of pore i; L_{ij} is the distance between pore i and pore j, m; g_{ij} is the fluid conductivity between neighboring pores, cm⁴/(MPa·s).

Applying the above equation to all pores and solving for the pressure of each pore under the given inlet and outlet pressures P_1 and P_0 , the volumetric flow rate q_{ij} between neighboring pores can be calculated. Finally, the total volumetric flow rate Q under the driving pressure difference (P_1-P_0) is determined. When gas and water phases coexist, the solution of pore pressure field is similar to that of single-phase flow, requiring only the conductivity coefficient of the respective fluid phase. After determining the

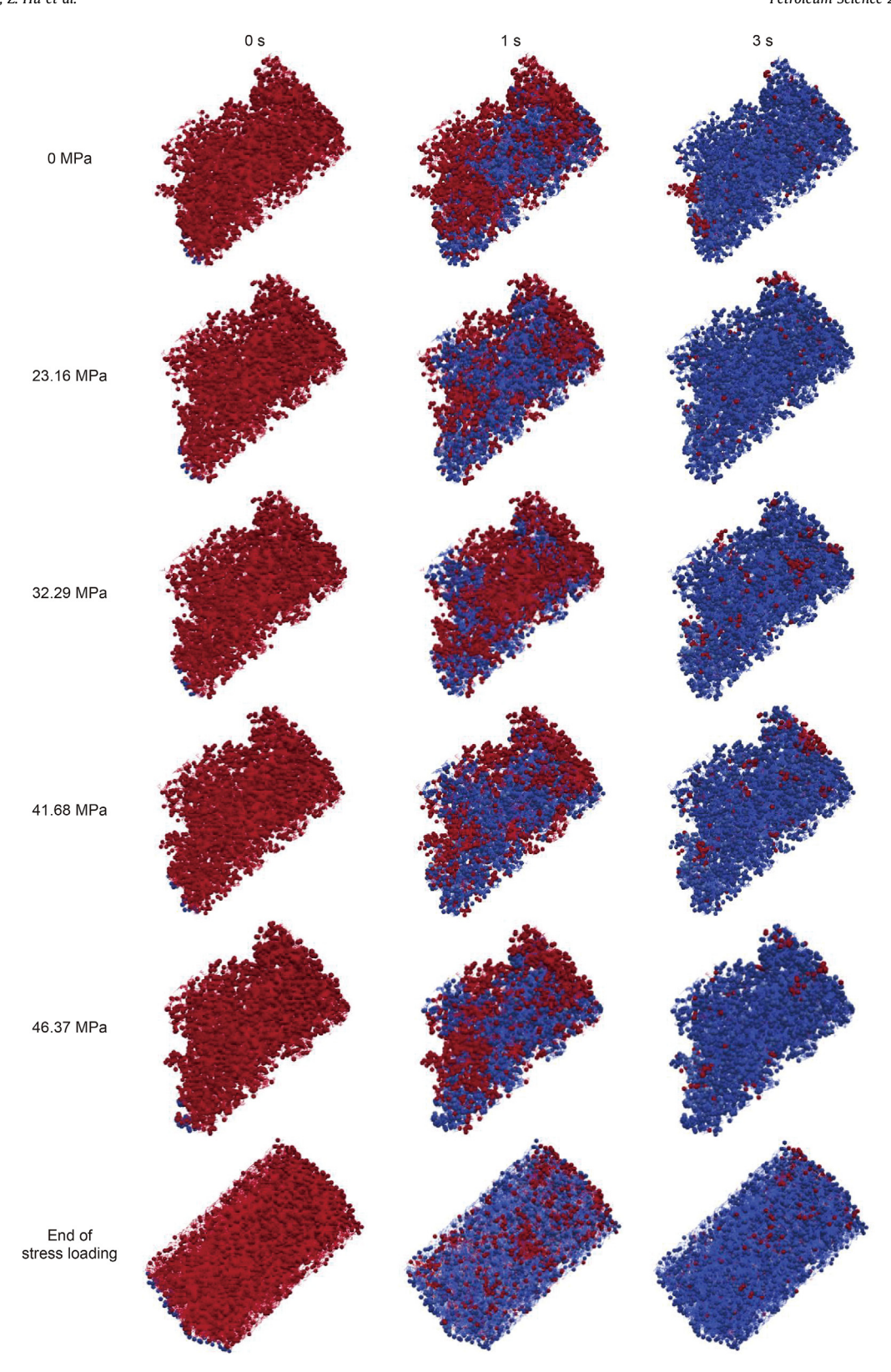


Fig. 10. Microscopic gas—water distribution ($K=10.07\times 10^{-3}~\mu m^2$).

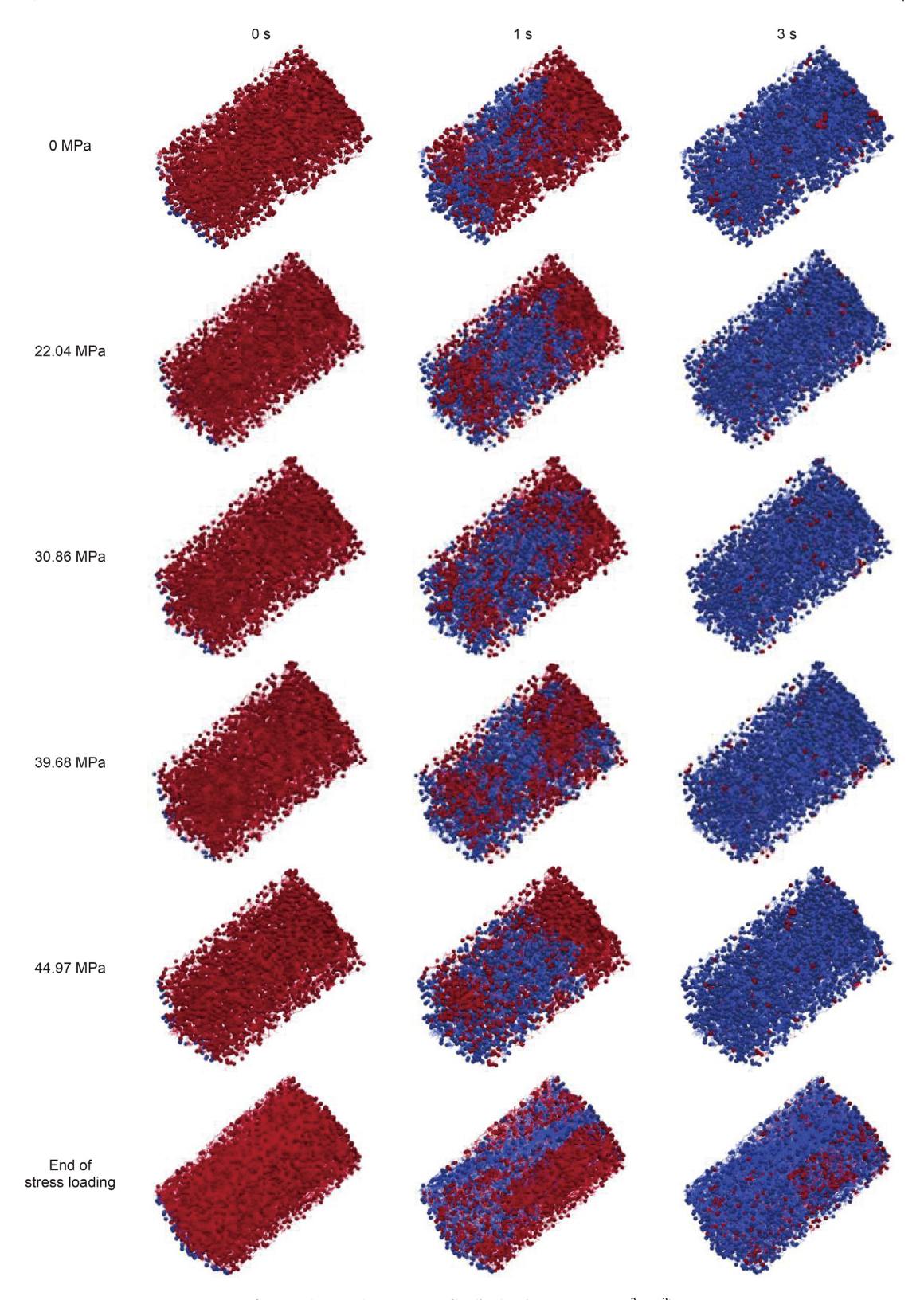
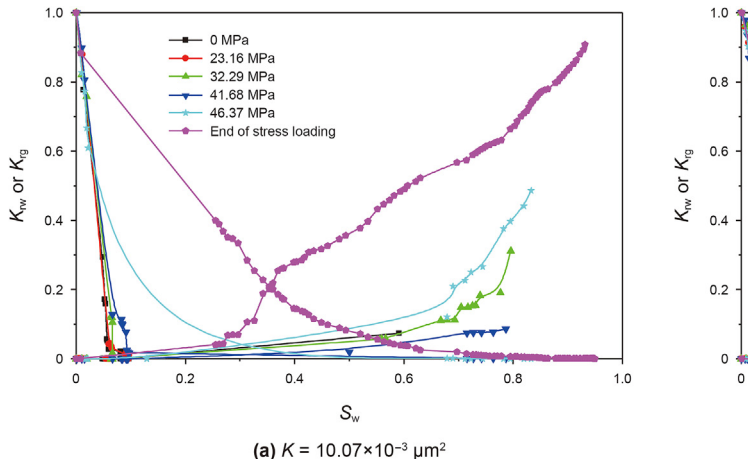


Fig. 11. Microscopic gas—water distribution ($K=57.75\times 10^{-3}~\mu m^2$).



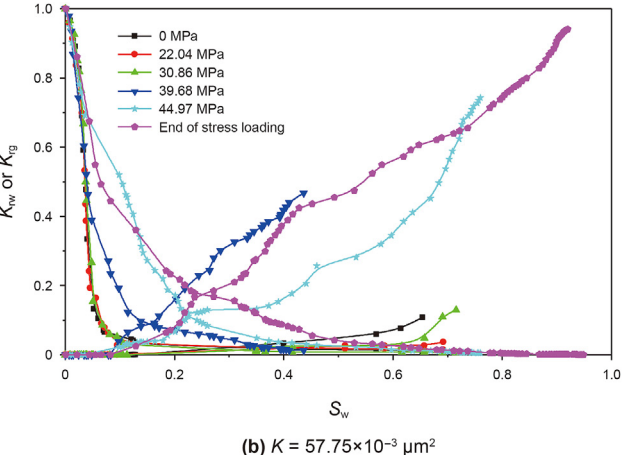


Fig. 12. Gas—water relative permeability curves estimated at different stress loading stages.

volumetric flow rate for each phase, the relative permeability K_{rp} of fluid phase p can be calculated:

$$K_{rp} = \frac{Q_{tmp}}{Q_{tsp}} \tag{6}$$

where $Q_{\rm tmp}$ is the volumetric flow rate of phase p under multiphase flow, cm³/s; $Q_{\rm tsp}$ is the total volumetric flow rate under single-phase flow, cm³/s.

After obtaining gas and water flow rates for each flow path, water saturation of the entire multi-scale model will be calculated using the following formula:

$$S_{W} = \frac{\sum_{i=1}^{n} V_{iW}}{\sum_{i=1}^{n} V_{i}}$$
 (7)

where n is the total number of pores and throats; V_i is the volume of pore or throat, cm³; V_{iw} is the volume of water in the pore or throat, cm³.

The quasi-static network simulations of gas—water two-phase flow is carried out for the pore network models under different dynamic load conditions. The microscopic distribution of gas—water at different effective stresses and simulation times is shown in Figs. 10 and 11.

The microscopic distribution of gas—water in low-permeability core ($K=10.07\times 10^{-3}~\mu m^2$) under different dynamic loading stages is shown in Fig. 10. In the early stage of stress loading, the water phase mainly flows along the well-connected pores in the middle of the model, with uneven water intrusion. The remaining gas is mainly distributed in the blind micro-pores. After the core ruptures, the fractures provide more flow channels for the gas, and the water phase quickly migrates to all types of pores.

The microscopic distribution of gas—water in high-permeability core ($K=57.75\times 10^{-3}~\mu m^2$) under different dynamic loading stages is shown in Fig. 11. In the early stage of stress loading, due to the obvious variation of pore size in the core, the non-uniform intrusion phenomenon is serious, forming a large amount of closed gas. When the stress is loaded to 39.68 MPa, the pore connectivity is enhanced, the sealing gas is reduced, and the migration speed of the water invasion front is accelerated. As the stress increases, the pore size heterogeneity becomes stronger, the gap between large and small pores becomes larger, and serious jamming and fingering phenomena occur, causing a decrease in water

invasion rate. During the core rupture stage, the water phase mainly flows along the pore throat with good connectivity in the middle of the model, forming a dominant flow channel, resulting in serious non-uniform water invasion.

Fig. 12 reflects the dynamic change in gas-water relative permeability curves of the deformed multi-scale fracture-porous media in both deep rocks under different dynamic loading stages. It can be seen that, in the linear elastic deformation stage, as the effective stress increases, the rock are gradually compacted, reducing the topological connectivity of deep rocks, decreasing the fluid flow paths, and lowering the relative permeability of water phase. After the rock is fractured, the generation of numerous micro-fractures significantly improves the topological connectivity inside the deep rocks, enhancing fluid conductivity and increasing relative permeability of gas phase and water phase. Compared with the deep rock with a permeability of $10.07 \times 10^{-3} \ \mu m^2$, the other deep rock with a permeability of $57.75 \times 10^{-3} \ \mu m^2$ has a shorter linear elastic deformation stage. When the in-situ stress reaches 39.68 MPa, numerous micro-fractures are formed within the rock, improving fluid conductivity and significantly increasing the relative permeability of water phase.

6. Conclusions

In this study, two actual deep rocks drilled from a typical ultradeep hydrocarbon reservoir in the Tarim Basin are used to conduct in-situ stress loading CT scanning experiments. Pore-scale network modeling is performed to reveal the microscopic gas—water two-phase flow behavior based on the accurate extraction of topologically equivalent deformed multi-scale fracture-pore network model under different dynamic loading stages. The main conclusions are as follows:

- (1) Through in-situ stress loading CT scanning experiments, slice images of deep rock microstructure at different dynamic loading stages are obtained. The U-Net deep learning semantic segmentation of rock skeleton, pore space, and fracture inside deep rock is then achieved, and 3D digital rock models of the deformable multi-scale media in deep rocks during different dynamic loading conditions are established.
- (2) Influenced by in-situ stress loading, both deep rocks mainly experience three stages: linear elastic deformation, plastic deformation, and shear failure. The evolution of mechanical behavior significantly affects the dynamic change of porethroat topological properties and gas—water two-phase

flow behavior in the deformed multi-scale fracture-porous media of deep rock.

- (3) In the linear elastic deformation stage, as the in-situ stress increases, both the deep rocks are gradually compacted and some micro-pores are closed, causing gradual decreases in average pore radius, pore-throat ratio, tortuosity and water-phase relative permeability, while the coordination number nearly remains unchanged. After the rocks are fractured, numerous micro-fractures and secondary pores are generated, greatly improving the topological connectivity and fluid conductivity, represented as sharp increases in average pore radius and coordination number, rapid decreases in pore-throat ratio and tortuosity, and remarkable enhancement in relative permeability of gas phase and water phase.
- (4) Compared with the deep rock with a permeability of $10.07 \times 10^{-3} \ \mu m^2$, the other deep rock with a permeability of $57.75 \times 10^{-3} \ \mu m^2$ typically has a shorter linear elastic deformation stage. When the in-situ stress reaches 39.68 MPa, microfractures begin to form within the rock, greatly increasing the fluid flow paths. The pore-throat ratio, coordination number, tortuosity, and water-phase relative permeability are gradually increased. Under the same stress loading stage, the better the rock properties, the higher the relative permeability of gas phase and water phase.

CRediT authorship contribution statement

Dai-Gang Wang: Writing — review & editing, Methodology. **Yu-Shan Ma:** Writing — original draft, Data curation. **Zhe Hu:** Visualization, Software. **Tong Wu:** Methodology, Investigation. **Ji-Rui Hou:** Visualization, Data curation. **Zhen-Chang Jiang:** Visualization, Software. **Xin-Xuan Qi:** Validation, Software. **Kao-Ping Song:** Supervision, Methodology. **Fang-Zhou Liu:** Writing — original draft, Software.

Conflict of interests

No conflict of interest exists in the submission of this manuscript, and manuscript is approved by all authors for publication. I would like to declare on behalf of my co-authors that the work is original research unpublished previously, and not under consideration for publication elsewhere, in whole or in part. All the authors listed have approved the manuscript enclosed.

Acknowledgments

This research is financially supported by the National Natural Science Foundation of China (No. 52174043), the Beijing Natural Science Foundation (No. 3242019), the CNPC Innovation Foundation (No. 2022DQ02-0208), and the State Key Laboratory of Deep Oil and Gas (No. SKLD0G2024-KFZD-06).

References

- Berg, C.F., Sahimi, M., 2023. Percolation and conductivity in evolving disordered media. Phys. Rev. 108 (2), 024132. https://doi.org/10.1103/PhysRevE.108.024132.
- Chen, R., Xu, Y., 2020. Threshold optimization selection of fast multimedia image segmentation processing based on LabVIEW. Multimed. Tool. Appl. 79, 9451–9467. https://doi.org/10.1007/s11042-019-07775-y.
- Cui, L.K., Sun, J.M., Yan, W.C., et al., 2020. Multi-scale and multi-component digital core construction and elastic property simulation. Appl. Geophys. 17 (1), 26–36. https://doi.org/10.1007/s11770-019-0789-7 (in Chinese).
- Dhamija, T., Gupta, A., Gupta, S., et al., 2023. Semantic segmentation in medical images through transfused convolution and transformer networks. Appl. Intell. 53 (1), 1132–1148. https://doi.org/10.1007/s10489-022-03642-w.
- Du, G., Cao, X., Liang, J., et al., 2020. Medical image segmentation based on U-Net: a review. J. Imag. Sci. Technol. 64 (2). https://doi.org/10.2352/

J.ImagingSci.Technol.2020.64.2.020508.

- Galkin, S.V., Martyushev, D.A., Osovetsky, B.M., et al., 2022. Evaluation of void space of complicated potentially oil-bearing carbonate formation using X-ray tomography and electron microscopy methods. Energy Rep. 8, 6245–6257. https://doi.org/10.1016/j.egyr.2022.04.070.
- Guo, B.E., Xiao, N., Martyushev, D., et al., 2024. Deep learning-based pore network generation: numerical insights into pore geometry effects on microstructural fluid flow behaviors of unconventional resources. Energy 294, 130990. https:// doi.org/10.1016/i.energy.2024.130990.
- Hao, F., 2022. Enrichment mechanism and prospects of deep oil and gas. Acta Geol. Sin. 96 (3), 742–756. https://doi.org/10.1111/1755-6724.14961.
- Huang, L., Baud, P., Cordonnier, B., et al., 2019. Synchrotron X-ray imaging in 4D: multiscale failure and compaction localization in triaxially compressed porous limestone. Earth Planet Sci. Lett. 528, 115831. https://doi.org/10.1016/ i.epsl.2019.115831.
- Ju, Y., Huang, Y., Gong, W., et al., 2018. 3-D reconstruction method for complex pore structures of rocks using a small number of 2-D X-ray computed tomography images. IEEE Trans. Geosci. Rem. Sens. 57 (4), 1873–1882. https://doi.org/ 10.1109/TGRS.2018.2869939.
- Khanna, A., Londhe, N.D., Gupta, S., et al., 2020. A deep residual U-Net convolutional neural network for automated lung segmentation in computed tomography images. Biocybern. Biomed. Eng. 40 (3), 1314–1327. https://doi.org/10.1016/ i.bbe.2020.07.007.
- Kornilov, A.S., Safonov, I.V., 2018. An overview of watershed algorithm implementations in open-source libraries. J. Imag. 4 (10), 123. https://doi.org/10.3390/ijmaging4100123.
- Lenoir, N., Bornert, M., Desrues, J., et al., 2007. Volumetric digital image correlation applied to X-ray microtomography images from triaxial compression tests on argillaceous rock. Strain 43 (3), 193–205. https://doi.org/10.1111/j.1475-1305.2007.00348.x.
- Liu, X., Chen, H., Chen, Z., et al., 2024. Study on characterization and distribution of four regions of tight sandstone condensate gas reservoirs in the depletion development process. Fuel 358, 130267. https://doi.org/10.1016/ ifuel_2023_130267.
- Ma, Y.S., Cai, X.Y., Li, M.W., et al., 2024. Research progress on the mechanisms of reservoir formation and hydrocarbon accumulation and the oil and gas development methods of deep and ultra-deep marine carbonates. Petrol. Explor. Dev. 51 (4), 1–16. https://doi.org/10.1016/S1876-3804(24)60507-0.
- Mao, L., Bi, Y., Liu, H., et al., 2023. Progress of internal deformation measurement of rock by using CT and digital volume correlation. Chin. Sci. Bull. 68 (4), 380–398. https://doi.org/10.1360/TB-2022-0405 (in Chinese).
- Martyushev, D.A., Ponomareva, I.N., Chukhlov, A.S., et al., 2023. Study of void space structure and its influence on carbonate reservoir properties: X-ray microtomography, electron microscopy, and well testing. Mar. Petrol. Geol. 151, 106192. https://doi.org/10.1016/j.marpetgeo.2023.106192.
- McBeck, J., Ben-Zion, Y., Renard, F., 2022. Volumetric and shear strain localization throughout triaxial compression experiments on rocks. Tectonophysics 822, 229181. https://doi.org/10.1016/j.tecto.2021.229181.
- Rassouli, F.S., Lisabeth, H., 2021. Analysis of time-dependent strain heterogeneity in shales using X-ray microscopy and digital volume correlation. J. Nat. Gas Sci. Eng. 92, 103984. https://doi.org/10.1016/j.jngse.2021.103984.
- Renard, F., McBeck, J., Cordonnier, B., et al., 2019. Dynamic in situ three-dimensional imaging and digital volume correlation analysis to quantify strain localization and fracture coalescence in sandstone. Pure Appl. Geophys. 176 (3), 1083—1115. https://doi.org/10.1007/s00024-018-2003-x.
- Saxena, N., Hofmann, R., Alpak, F.O., et al., 2017. Effect of image segmentation & voxel size on micro-CT computed effective transport & elastic properties. Mar. Petrol. Geol. 86, 972–990. https://doi.org/10.1016/j.marpetgeo.2017.07.004.
- Shi, H.L., Hosdez, J., Rougelot, T., et al., 2021. Analysis of local creep strain field and cracking process in claystone by X-ray micro-tomography and digital volume correlation. Rock Mech. Rock Eng. 54 (4), 1937–1952. https://doi.org/10.1007/ s00603-021-02375-5.
- Su, Y.L., Xu, J.L., Wang, W.D., et al., 2022. Relative permeability estimation of oil—water two-phase flow in shale reservoir. Pet. Sci. 19 (3), 1153—1164. https:// doi.org/10.1016/j.petsci.2021.12.024.
- Sun, H., Belhaj, H., Tao, G., et al., 2019. Rock properties evaluation for carbonate reservoir characterization with multi-scale digital rock images. J. Petrol. Sci. Eng. 175, 654–664. https://doi.org/10.1016/j.petrol.2018.12.075.
- Sun, J.S., Xu, C.Y., Kang, Y.L., et al., 2020. Research progress and development recommendations covering damage mechanisms and protection technologies for tight/shale oil and gas reservoirs. Petroleum Drilling Techn. 48 (4), 1–9. https://doi.org/10.11911/syztjs.2020068 (in Chinese).
- Sun, L.D., Zou, C.N., Zhu, R.K., et al., 2013. Formation, distribution and potential of deep hydrocarbon resources in China. Petrol. Explor. Dev. 40, 641–649. https:// doi.org/10.1016/S1876-3804(13)60093-2.
- Tan, M., Su, M., Liu, W., et al., 2021. Digital core construction of fractured carbonate rocks and pore-scale analysis of acoustic properties. J. Petrol. Sci. Eng. 196, 107771. https://doi.org/10.1016/j.petrol.2020.107771.
- Van Stappen, J.F., Meftah, R., Boone, M.A., et al., 2018. In situ triaxial testing to determine fracture permeability and aperture distribution for CO₂ sequestration in Svalbard, Norway. Environ. Sci. Technol. 52 (8), 4546–4554. https://doi.org/10.1021/acs.est.8b00861.
- Verri, I., Della Torre, A., Montenegro, G., et al., 2017. Development of a digital rock physics workflow for the analysis of sandstones and tight rocks. J. Petrol. Sci. Eng. 156, 790–800. https://doi.org/10.1016/j.petrol.2017.06.053.

- Wang, D.G., Wang, C.C., Li, C.F., et al., 2018. Effect of gas hydrate formation and decomposition on flow properties of fine-grained quartz sand sediments using X-ray CT based pore network model simulation. Fuel 226, 516—526. https://doi.org/10.1016/j.fuel.2018.04.042.
- Wang, D.G., Wei, W., Sun, J.J., et al., 2020. Dynamic evolution of pore structures of hydrate-bearing sediments induced by step-wise depressurization. Chin. Sci. Bull. 65, 2292–2302. https://doi.org/10.1360/TB-2020-0010 (in Chinese).
- Wang, D.G., Liu, F.Z., Sun, J.J., et al., 2023. Lattice-Boltzmann simulation of two-phase flow in carbonate porous media retrieved from computed microtomography. Chem. Eng. Sci. 270, 118514. https://doi.org/10.1016/j.ces.2023.118514.
- Wang, H.T., Li, W., Liu, F.Q., et al., 2020. Investigation of image segmentation effect on the accuracy of reconstructed digital core models of coquina carbonate. Appl. Geophys. 17, 501–512. https://doi.org/10.1007/s11770-020-0846-2 (in Chinese).
- Wang, R.J., Tang, Y.L., Zhu, S.B., et al., 2024. Numerical simulation of multi-scale coupled flow in ultra-deep fractured tight sandstone gas reservoirs. Nat. Gas. Ind. 44 (3), 143–151. https://doi.org/10.3390/min14070686.
- Yao, J., Huang, Z.Q., Liu, W.Z., et al., 2018. Key mechanical problems in the development of deep oil and gas reservoirs. Sci. China Phys. Mech. Astron. 48,

- 044701. https://doi.org/10.1360/SSPMA2017-00286 (in Chinese).
- Yao, J., Huang, Z.Q., Sun, H., et al., 2023. Research progress of multi-scale methods for oil and gas flow in porous media. Petroleum Science Bulletin 1, 32–68. https://doi.org/10.3969/j.issn.2096-1693.2023.01.004 (in Chinese).
- Zhang, J., Niu, Y., Shangguan, Z., et al., 2023. A novel denoising method for CT images based on U-net and multi-attention. Comput. Biol. Med. 152, 106387. https://doi.org/10.1016/j.compbiomed.2022.106387.
- Zhang, T., Salama, A., Sun, S., et al., 2015. Pore network modeling of drainage process in patterned porous media: a quasi-static study. J. Comput. Sci. 9, 64–69. https://doi.org/10.1016/j.jocs.2015.04.010.
- Zhang, Y., Lu, H., Rong, J., et al., 2017. Adaptive non-local means on local principle neighborhood for noise/artifacts reduction in low-dose CT images. Med. Phys. 44 (9), e230–e241. https://doi.org/10.1002/mp.12388.
 Zhang, Y., Salehjahromi, M., Yu, H., 2019. Tensor decomposition and non-local
- Zhang, Y., Salehjahromi, M., Yu, H., 2019. Tensor decomposition and non-local means based spectral CT image denoising. J. X Ray Sci. Technol. 27 (3), 397–416. https://doi.org/10.3233/XST-180413.
- Zhao, B., MacMinn, C.W., Primkulov, B.K., et al., 2019. Comprehensive comparison of pore-scale models for multiphase flow in porous media. Proc. Natl. Acad. Sci. USA 116 (28), 13799–13806. https://doi.org/10.1073/pnas.1901619116.